Ballistic Electron Source with Magnetically Controlled Valley Polarization in Bilayer Graphene

Ingla-Aynés, Josep; Manesco, Antonio L.R.; Ghiasi, Talieh S.; Watanabe, Kenji; Taniguchi, Takashi; Van Der Zant, Herre S.J.

DOI
10.1103/PhysRevLett.133.156301

Publication date
2024

Document Version
Final published version

Published in
Physical review letters

Editors' Suggestion

Ballistic Electron Source with Magnetically Controlled Valley Polarization in Bilayer Graphene

Josep Ingla-Aynés,[1,*] Antonio L. R. Manesco,[1] Talieh S. Ghiasi,[1] Kenji Watanabe,[2]
Takashi Taniguchi,[3] and Herre S. J. van der Zant[1]
[1]*Kavli Institute of Nanoscience, Delft University of Technology, Lorentzweg 1, 2628 CJ Delft, The Netherlands*
[2]*Research Center for Electronic and Optical Materials, National Institute for Materials Science, 1-1 Namiki, Tsukuba 305-0044, Japan*
[3]*Research Center for Materials Nanoarchitectonics, National Institute for Materials Science, 1-1 Namiki, Tsukuba 305-0044, Japan*

(Received 9 November 2023; revised 20 July 2024; accepted 18 August 2024; published 11 October 2024)

The achievement of valley-polarized electron currents is a cornerstone for the realization of valleytronic devices. Here, we report on ballistic coherent transport experiments where two opposite quantum point contacts (QPCs) are defined by electrostatic gating in a bilayer graphene (BLG) channel. By steering the ballistic currents with an out-of-plane magnetic field we observe two current jets, a consequence of valley-dependent trigonal warping. Tuning the BLG carrier density and number of QPC modes (m) with a gate voltage we find that the two jets are present for $m = 1$ and up to $m = 6$, indicating the robustness of the effect. Semiclassical simulations confirm the origin of the signals by quantitatively reproducing the jet separations without fitting parameters. In addition, our model shows that the ballistic current jets have opposite valley polarization. As a consequence, by steering each jet toward the detector using a magnetic field, we achieve full control over the valley polarization of the collected currents, envisioning such devices as ballistic current sources with tunable valley polarization. We also show that collimation experiments are a sensitive probe to the trigonal warping of the Fermi surface.

DOI: 10.1103/PhysRevLett.133.156301

A functional valleytronic device requires controllable injection of valley-polarized currents [1–6]. Thus, ballistic valley splitters, which enable current sources with magnetic-field tunable valley polarization, are crucial components of valleytronic devices. Bernal stacked bilayer graphene (BLG) is a unique material platform for a valley splitter [7–11]. Its gate-tunable band gap allows the fabrication of nanodevices free of intervalley scattering [12–15]. Furthermore, trigonal warping, i.e., triangular distortion of its Fermi surface, is valley dependent [16] [see Fig. 1(a)]. Such a band structure makes quantum point contacts (QPCs) emit valley-polarized ballistic electron jets [16–22]. Despite early theoretical proposals, it is only recently that the current jets have been mapped by scanning gate measurements [23] in an electrostatically defined QPC in BLG [24–32]. This is due to the stringent requirements of coherent injection by a QPC with significant trigonal warping [21,23,33].

Recent transverse electron focusing experiments [34] between gate-defined QPCs in BLG showed signatures of valley-resolved ballistic transport. However, as they require a significant electron deflection by the magnetic field, a large fraction of the Fermi surface is probed, and most of the trigonal warping effects are averaged out. In this context, a ballistic measurement setup where electrons are deflected only by small angles [35–38] would unambiguously probe the ballistic valley-polarized electron jets [see Fig. 1(b)], opening the way for new valley-polarized electron sources with magnetic-field-controlled polarization.

Here, we perform ballistic collimation experiments where two electrostatically defined QPCs are placed opposing each other [see Fig. 1(c)], and the electrons are steered toward the detector using an out-of-plane magnetic field (B). The measurements show the formation of two ballistic current jets independently of the number of QPC modes (m). Using semiclassical simulations that predict the formation of valley-polarized current jets, we reproduce the jet separation without the need for any fitting parameter and show a high sensitivity to the degree of trigonal warping of the Fermi surface. These observations confirm that, when current-biased, the measured devices operate like magnetic-field controlled valley-polarized ballistic current sources, as illustrated in Figs. 1(d) and 1(e).

Our valley-polarized electron sources are in a Van der Waals heterostructure consisting of a BLG flake encapsulated between an upper and a lower hBN flake with thicknesses 28 and 23 nm, respectively. The stack is placed on a multilayer graphene back gate [24]. The device, which is shown in Fig. 1(c), contains multiple contacts to the BLG flake (red) and 50-nm-separated split gates on the top hBN (yellow); see Ref. [34] for fabrication details.

We first investigate the QPC formation. By applying a bias current ($I_1 = 100$ nA) to QPC1 and monitoring the

*Contact author: jingla@mit.edu

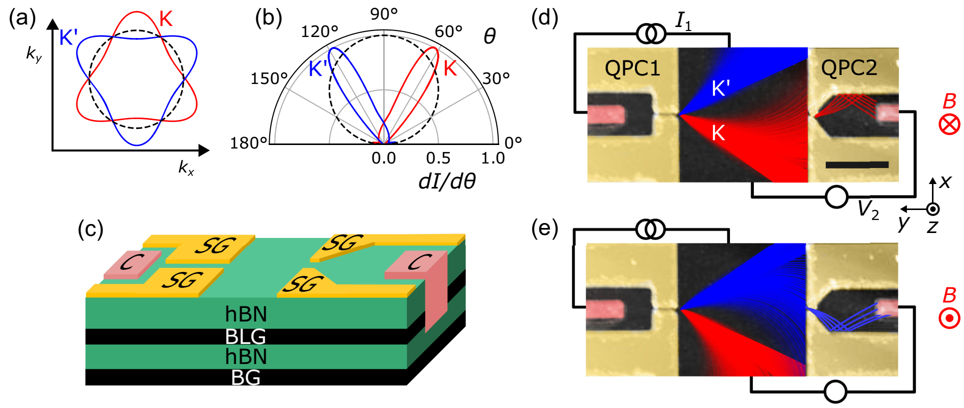

FIG. 1. Trigonal warping, valley splitter, and magnetically controlled valley-polarized current source in bilayer graphene. (a) Fermi surface of BLG in valley K (red) and K' (blue). A circular Fermi surface (black dashed line) is shown for comparison. (b) Angular distribution ($dI/d\theta$) of the valley-polarized current jets emitted by a quantum point contact in BLG, showing that QPC1 is a valley splitter. The dashed black line corresponds to the circular Fermi surface case where the distribution is $\cos(\theta)$. (c) Device sketch where the contacts to BLG (C) are light red, the split gates (SG) are yellow, the multilayer graphene back gate (BG) and the BLG are black and the boron nitride (hBN) is green. Additional contacts to BLG were placed far from the SG structure for the collimation experiments. (d) False color atomic force microscopy image of the measured device where the split gates, that define the QPCs by preventing electron transport in the covered areas, are yellow and the contacts to BLG are light red. The scale bar is 2 μm. The red and blue lines represent valley-polarized electron trajectories calculated under a small negative magnetic field (B). Note that $\theta = 0$ in panel b corresponds to $-x$ here and in the subsequent device sketches. Reversing B results in the trajectories shown in (e). In panel (d), only electrons in valley K reach the detector island. In contrast, in panel (e), only K' electrons are collected, illustrating the B-controlled valley filter operation.

two-terminal voltage [V_1, right inset of Fig. 2(b)] as a function of the back gate voltage (V_{bg}) and the voltage applied to the split gates (V_{tg}), we obtain the resistance map in Fig. 2(a), where $R_1 = V_1/I_1$. The vertical line at $V_{bg} \approx 0$ corresponds to the charge neutrality point of the non-top-gated BLG regions and shows that the residual doping is very small. The diagonal line corresponds to the charge neutrality point of the double-gated region and gives rise to a maximal R_1 at each V_{bg} [$R_{max}(V_{bg})$]. For $V_{bg} > 0$, $R_{max}(V_{bg})$ increases with increasing V_{bg} until $V_{bg} \approx 0.8$ V, after which it starts decreasing. This is due to the formation of a QPC between the split gates with increasing carrier density (n).

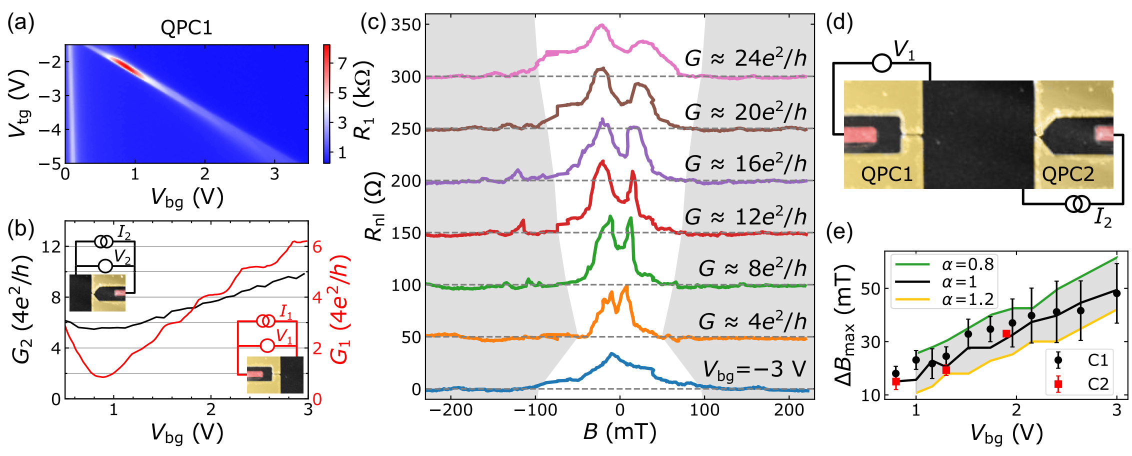

FIG. 2. Steering of current jets emitted by a QPC using an out-of-plane magnetic field at 1.8 K. (a) Two-terminal resistance measured across QPC1 [right inset in panel (b)] as a function of the back-gate (V_{bg}) and split-gate (V_{tg}) voltages. (b) Conductance of QPC1 (red line, right axis and right inset circuit) and QPC2 (black line, left axis and left inset circuit). (c) Collimation experiments at different V_{bg}. The positive V_{bg} values correspond to quantized G and are labeled accordingly. The gray areas mark the B range where the average diameter of the cyclotron orbit is smaller than the QPC separation and no signal is expected. The curves are offset 50 Ω, as shown by the dashed lines. An offset in B was added to correct for the magnet remanence. (d) Measurement geometry corresponding to the collimation experiments in panel (c). (e) Peak separation ΔB_{max} vs V_{bg}. The black circles are extracted from panel (c); the red squares are obtained from measurements on a second pair of QPCs (C2). The black solid line is obtained from the model described in the main text and in Fig. 3 for $\alpha = 1$ (the gray area corresponds to $0.8 < \alpha < 1.2$). The error bars are estimated from the peak widths.

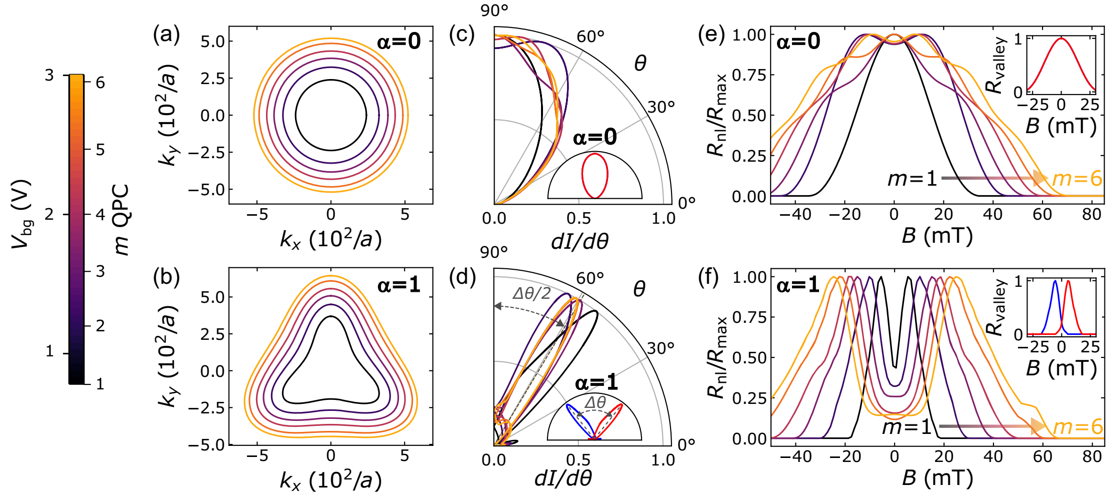

FIG. 3. Semiclassical simulations and the role of trigonal warping for increasing QPC mode number ($m = 1, 2, \ldots, 6$). All the curves (apart from the insets, that are colored based on the valley index) are color coded according to the left color bar. (a),(b) Fermi surfaces, (c),(d) angular distribution of emitted currents $dI/d\theta$, and (e),(f) the simulated collimation spectra without ($\alpha = 0$) and with ($\alpha = 1$) trigonal warping, respectively. In panel (d), $\Delta\theta$ is the angular separation between $dI/d\theta$ peaks. Ignoring the valley polarization, $dI/d\theta$ in panels (c) and (d) is symmetric with respect to $\theta = 90°$. The insets show the corresponding valley-resolved signal at $V_{bg} = 0.8$ V, with a single QPC mode. In panels a and b, $a = \sqrt{3}a_0$, where a_0 is the in-plane separation between carbon atoms.

To find if the QPC conductance (G) is quantized, we determine it using $G(V_{bg}) = [R_{max}(V_{bg}) - R_{min}(V_{bg})]^{-1}$, where $R_{min}(V_{bg})$ is the minimal resistance at each V_{bg} which is dominated by the contact resistances. The result is shown in Fig. 2(b) by the red line and shows plateaus at $G = m \times 4e^2/h$, where $m = 1, \ldots, 6$ for $V_{bg} > 0$, indicating the formation of a spin- and valley-degenerate QPC with m modes [26,27]. As shown in Ref. [39], for $V_{bg} < 0$ $G \approx 8 \times 4e^2/h$ and is not quantized. To characterize QPC2, we use the black circuit in the left inset of Fig. 2(b) and, applying a current I_2, we obtain $R_2 = V_2/I_2$ and subtract the contact resistances as above to obtain G_2, that is plotted as the drawn black line in Fig. 2(b). It does not show size quantization steps, neither for electron nor hole transport [39]. Henceforth, to ensure that charge transport occurs only through the gate-defined QPCs between the split gates, V_{tg} has been adjusted to the diagonal line in Fig. 2(a) (charge neutrality of the split-gated regions).

To determine the angular distribution of the charge current emitted by the QPCs, we have measured V_1 while applying a current $I_2 = 100$ nA across QPC2 [black circuit in Fig. 2(d)]. As shown below, this configuration is equivalent to Fig. 1(d). The nonlocal resistance $R_{nl} = V_1/I_2$ is plotted vs B at different V_{bg} in Fig. 2(c) and, for positive V_{bg} (quantized G), shows two clear peaks for all the measured V_{bg}. In contrast, at $V_{bg} = -3$ V and for all the measured $V_{bg} < 0$ values, even though a structure consistent with two broadened current jets can be distinguished, only a single peak is observed [39].

To further understand the measured signals, we quantify the B separation between R_{nl} peaks (ΔB_{max}), which is shown in Fig. 2(e) vs V_{bg} for $V_{bg} > 0$. In this figure, ΔB_{max} increases with n. Note that, in addition to the data obtained from the QPCs in Fig. 2(d) that we call C1, we have also measured collimation between a second pair of QPCs aligned along the same crystallographic direction, which we call C2 [39]. ΔB_{max} obtained from C2 is shown as the red dots in Fig. 2(e) and shows good agreement with C1. It is worth noting that, even though the emission of current jets has shown stability against small variations in the electric field [23], how it will evolve when $m > 1$ QPC modes contribute to the angular distribution of emitted currents remains a question. In the absence of trigonal warping, the higher modes give rise to extra lobes in the collimation [37,40], but their effect in the presence of trigonal warping remains unknown to this point. The results in Fig. 2 show that the peak spacing widens as the number of modes of the detector QPC increases from 1 to 6. The absence of other clear changes indicates that the presence of high-order QPC modes does not prevent current jetting.

We study the origin of the double-peak feature in R_{nl} with semiclassical simulations. Under an applied magnetic field, the electron trajectories are cyclotronic orbits written as $l_B^2 k_F(\phi + \pi/2)$, where $l_B^2 = \hbar/qB$, $\hbar$ is the reduced Planck's constant, $k_F(\phi)$ the Fermi surface, obtained from [16,41], $\phi = \arctan(k_y/k_x)$ the polar angle [see Fig. 3(b)], and q the effective carrier charge. Accordingly, quasiparticles rotate clockwise or counterclockwise depending on the sign of B and q ($q = e$ for electrons and $q = -e$ for holes) [42]. The contribution of each orbit to the collected current is determined by two factors. First, the injection probability $dI/d\theta$, which depends on the injection angle θ and accounts for trigonal warping and size quantization. Second, the collection probability, that accounts for the absence of size quantization in QPC2, the detection point, angle, and trigonal warping. Given the high carrier density in the single-gated region, Berry curvature effects are disregarded. We vary the trigonal warping strength with the parameter α: $\alpha = 0$ amounts to a circular Fermi surface [Fig. 3(a)], whereas $\alpha = 1$ results in the fully warped Fermi surface [Fig. 3(b)] calculated using the parameters obtained in Ref. [41]. The model is described in Ref. [39] and the code used for the simulations is available in Ref. [47].

Because in the absence of trigonal warping the Fermi surface is isotropic, $dI/d\theta$ is equal for both valleys [Fig. 3(c), inset]. As illustrated in Fig. 3(c), for $\alpha = 0$ and $m > 1$, size quantization results in multiple collimation lobes [37,40]. In contrast, for a fully warped Fermi surface [Fig. 3(d)] $dI/d\theta$ becomes valley dependent and the double jetting persists regardless of the number of modes, in agreement with Ref. [21]. Note that the exact separation between the $dI/d\theta$ peaks ($\Delta\theta$) is sensitive to V_{bg}. This result implies that the current jet formation is sensitive to the electric field and/or carrier density at the QPC. We explain it considering that the Fermi surfaces are not perfect triangles and changing the k-dependent occupation of the electron states can influence the current jet orientation. This result is consistent with our observation that, at fixed V_{bg}, variations in V_{tg} [that influence the electric field at the QPC but not the ballistic transport in the black areas of Fig. 2(d)] change the peak positions up to 10 mT at $V_{\mathrm{bg}} = 1.3$ V [39]. Such an influence of size quantization on $dI/d\theta$ agrees with our simulations [39] and indicates that, for wide and high-m QPCs, as expected for $V_{\mathrm{bg}} < 0$, where $G \approx 8 \times 4e^2/h$, the peaks broaden. This explains the collimation spectra measured in this range where the negative-B peak is broader than the peak separation [39].

Finally, we compute the current absorbed in the collector. Comparing Figs. 3(e) and 3(f), we find that the double-peak feature occurs for the whole V_{bg} range only with a warped Fermi surface. Furthermore, as in the experiment, the peak spacing obtained with a fully warped surface increases with V_{bg}. This change in the peak spacing occurs due to the increase of the Fermi surface as the electron density increases [Fig. 3(b)]. We extracted the peak separation from Fig. 3(f) and plotted it vs V_{bg} in Fig. 2(e) as a black solid line. The agreement between the model with $\alpha = 1$ and the experimental results presents compelling evidence that the measured signals are caused by valley-polarized current jets. We stress the absence of fitting parameters in this comparison and that all the relevant parameters in the model originate from independent measurements on the same sample and tight-binding parameters obtained by infrared spectroscopy [41]. The gray area in Fig. 2(e) shows ΔB_{max} for $0.8 < \alpha < 1.2$ and demonstrates the sensitivity of the peak separation to the degree of trigonal warping.

The experimental data [see Fig. 2(c)] also shows an asymmetry of the R_{nl} peak widths. While the spectra calculated in Fig. 3 assume a perfect alignment of the QPCs with the BLG crystal planes ($\delta = 0$) and perfectly opposing QPCs ($\Delta y = 0$), see the left insets of Fig. 4 for the definitions of Δy and δ, these assumptions are unlikely to be fulfilled in practice. We have extended the model in Ref. [39] to account for $\delta \neq 0$ and $\Delta y \neq 0$ and realized that both can lead to asymmetry in the peaks, in width and height. This result shows that small misalignments can be the reason for the observed peak asymmetry.

We have also investigated the temperature (T) dependence of the double-peak structure. Such an experiment has been performed at $V_{\mathrm{bg}} = 1.3$ V corresponding to $G = 8e^2/h$ and the results are shown in Fig. 4. Note that, by swapping the I-source and V-measurement units with respect to Fig. 3 (Fig. 4, inset), the B asymmetry of R_{nl} changes sign, confirming that the I source does not affect the current jet formation and our measurements obey reciprocity [48,49]. Besides a very clear peak width asymmetry, R_{nl} also shows a slow decay as T increases, leading to the observation of the two peaks up to 40 K. Above this temperature, R_{nl} becomes negative at $|B| \approx 0.1$ T. The negative signal measured for $T \geq 50$ K can be due to a significant portion of the current propagating across the double-gated regions,

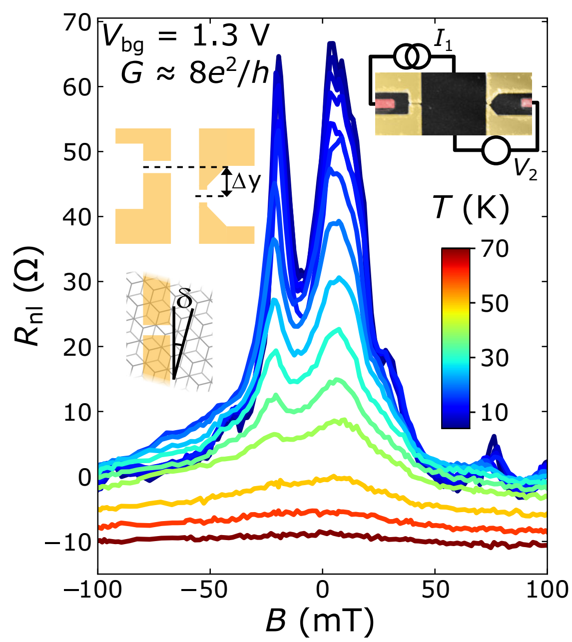

FIG. 4. Temperature dependence of ballistic electron jetting at $V_{\mathrm{bg}} = 1.3$ V. The line colors indicate the measurement temperature as illustrated by the color bar. The curves are offset in B to correct for the magnet remanence. The right inset shows the measurement geometry, which is the reciprocal of Fig. 2. As a consequence, the B asymmetry shows opposite behavior. The left insets illustrate the misalignment between QPCs (Δy) and the rotation between the BLG armchair axis and the split gates (δ) used to explain the peak asymmetry.

diffusive charge transport between the injector and collector, and viscous flow of electrons [50,51]. Furthermore, the observed T dependence of the double peak near $B = 0$ confirms that it is not caused by quantum interference between ballistic trajectories, as the phase coherence length in BLG is expected to decrease quickly with increasing T, suppressing interference effects [43] above 10 K (see Ref. [39] for a more detailed analysis).

To conclude, we have performed collimation experiments between electrostatically defined QPCs and detected ballistic electron jets. Using semiclassical simulations, we show that the origin of the measured spectra lies in the trigonal warping of the Fermi surface, implying the valley polarization of the current jets. In addition, the demonstrated sensitivity of the collimation spectra to the trigonal warping of the Fermi surface makes such experiments a unique probe to the Fermi surface shape. The realization of a valley-polarized current source with controllable polarization is promising for the future of valleytronic devices operating in the classical [52] and quantum [53] regimes. This approach might also be used to generate spin-valley polarized currents in transition metal dichalcogenides [21], where QPCs have already been realized [54,55].

Note added—We recently became aware of two related experimental works on valley transport in BLG [56,57].

Acknowledgments—We thank A. Akhmerov, K. Vilkelis, and M. Bozkurt for insightful discussions. This project received funding from the European Union Horizon 2020 research and innovation program under Grant Agreement No. 863098 (SPRING) and Marie Sklodowska-Curie individual fellowship No. 101027187-PCSV awarded to J. I. A. A. L. R. M. work was supported by VIDI Grant No. 016.Vidi.189.180. K. W. and T. T. acknowledge support from JSPS KAKENHI (Grants No. 21H05233 and No. 23H02052) and World Premier International Research Center Initiative (WPI), MEXT, Japan.

Data availability—All the data and code associated with the analysis and theoretical simulations are available from Ref. [47].

J. I. A., A. L. R. M., and H. S. J .vdZ. conceived the project. JIA performed the measurements with help from TSG. ARLM performed the simulations with help from J. I. A. K. W. and T. T. synthesized the hexagonal boron nitride crystals. J. I. A. wrote the manuscript with input from all authors. H. S. J .vdZ. supervised the project.

[1] J. R. Schaibley, H. Yu, G. Clark, P. Rivera, J. S. Ross, K. L. Seyler, W. Yao, and X. Xu, Valleytronics in 2d materials, Nat. Rev. Mater. **1**, 1 (2016).

[2] Z.-M. Yu, S. Guan, X.-L. Sheng, W. Gao, and S. A. Yang, Valley-layer coupling: A new design principle for valleytronics, Phys. Rev. Lett. **124**, 037701 (2020).

[3] M. Sui, G. Chen, L. Ma, W.-Y. Shan, D. Tian, K. Watanabe, T. Taniguchi, X. Jin, W. Yao, D. Xiao *et al.*, Gate-tunable topological valley transport in bilayer graphene, Nat. Phys. **11**, 1027 (2015).

[4] Y. Shimazaki, M. Yamamoto, I. V. Borzenets, K. Watanabe, T. Taniguchi, and S. Tarucha, Generation and detection of pure valley current by electrically induced berry curvature in bilayer graphene, Nat. Phys. **11**, 1032 (2015).

[5] S. Roche, S. R. Power, B. K. Nikolić, J. H. García, and A.-P. Jauho, Have mysterious topological valley currents been observed in graphene superlattices?, J. Nonlinear Opt. Phys. Mater. **5**, 021001 (2022).

[6] A. Aharon-Steinberg, A. Marguerite, D. J. Perello, K. Bagani, T. Holder, Y. Myasoedov, L. S. Levitov, A. K. Geim, and E. Zeldov, Long-range nontopological edge currents in charge-neutral graphene, Nature (London) **593**, 528 (2021).

[7] I. Martin, Y. M. Blanter, and A. F. Morpurgo, Topological confinement in bilayer graphene, Phys. Rev. Lett. **100**, 036804 (2008).

[8] P. San-Jose, E. Prada, E. McCann, and H. Schomerus, Pseudospin valve in bilayer graphene: Towards graphene-based pseudospintronics, Phys. Rev. Lett. **102**, 247204 (2009).

[9] J. Li, K. Wang, K. J. McFaul, Z. Zern, Y. Ren, K. Watanabe, T. Taniguchi, Z. Qiao, and J. Zhu, Gate-controlled topological conducting channels in bilayer graphene, Nat. Nanotechnol. **11**, 1060 (2016).

[10] J. Li, R.-X. Zhang, Z. Yin, J. Zhang, K. Watanabe, T. Taniguchi, C. Liu, and J. Zhu, A valley valve and electron beam splitter, Science **362**, 1149 (2018).

[11] J. Yin, C. Tan, D. Barcons-Ruiz, I. Torre, K. Watanabe, T. Taniguchi, J. C. Song, J. Hone, and F. H. Koppens, Tunable and giant valley-selective Hall effect in gapped bilayer graphene, Science **375**, 1398 (2022).

[12] E. V. Castro, K. S. Novoselov, S. V. Morozov, N. M. R. Peres, J. M. B. L. Dos Santos, J. Nilsson, F. Guinea, A. Geim, and A. C. Neto, Biased bilayer graphene: Semiconductor with a gap tunable by the electric field effect, Phys. Rev. Lett. **99**, 216802 (2007).

[13] J. B. Oostinga, H. B. Heersche, X. Liu, A. F. Morpurgo, and L. M. Vandersypen, Gate-induced insulating state in bilayer graphene devices, Nat. Mater. **7**, 151 (2008).

[14] Y. Zhang, T.-T. Tang, C. Girit, Z. Hao, M. C. Martin, A. Zettl, M. F. Crommie, Y. R. Shen, and F. Wang, Direct observation of a widely tunable bandgap in bilayer graphene, Nature (London) **459**, 820 (2009).

[15] E. Icking, L. Banszerus, F. Wörtche, F. Volmer, P. Schmidt, C. Steiner, S. Engels, J. Hesselmann, M. Goldsche, K. Watanabe *et al.*, Transport spectroscopy of ultraclean tunable band gaps in bilayer graphene, Adv. Electron. Mater. **8**, 2200510 (2022).

[16] E. McCann and M. Koshino, The electronic properties of bilayer graphene, Rep. Prog. Phys. **76**, 056503 (2013).

[17] J. L. Garcia-Pomar, A. Cortijo, and M. Nieto-Vesperinas, Fully valley-polarized electron beams in graphene, Phys. Rev. Lett. **100**, 236801 (2008).

[18] Z. Wang and F. Liu, Manipulation of electron beam propagation by hetero-dimensional graphene junctions, ACS Nano **4**, 2459 (2010).

[19] D. R. Da Costa, A. Chaves, S. H. R. Sena, G. A. Farias, and F. M. Peeters, Valley filtering using electrostatic potentials in bilayer graphene, Phys. Rev. B **92**, 045417 (2015).

[20] T. Stegmann and N. Szpak, Current splitting and valley polarization in elastically deformed graphene, 2D Mater. **6**, 015024 (2018).

[21] A. L. Manesco and A. Pulkin, Spatial separation of spin currents in transition metal dichalcogenides, SciPost Phys. Core **6**, 036 (2023).

[22] L. Seemann, A. Knothe, and M. Hentschel, Gate-tunable regular and chaotic electron dynamics in ballistic bilayer graphene cavities, Phys. Rev. B **107**, 205404 (2023).

[23] C. Gold, A. Knothe, A. Kurzmann, A. Garcia-Ruiz, K. Watanabe, T. Taniguchi, V. Fal'ko, K. Ensslin, and T. Ihn, Coherent jetting from a gate-defined channel in bilayer graphene, Phys. Rev. Lett. **127**, 046801 (2021).

[24] H. Overweg, H. Eggimann, X. Chen, S. Slizovskiy, M. Eich, R. Pisoni, Y. Lee, P. Rickhaus, K. Watanabe, T. Taniguchi *et al.*, Electrostatically induced quantum point contacts in bilayer graphene, Nano Lett. **18**, 553 (2018).

[25] R. Kraft, J. Mohrmann, R. Du, P. B. Selvasundaram, M. Irfan, U. N. Kanilmaz, F. Wu, D. Beckmann, H. Von Löhneysen, R. Krupke *et al.*, Tailoring supercurrent confinement in graphene bilayer weak links, Nat. Commun. **9**, 1722 (2018).

[26] H. Overweg, A. Knothe, T. Fabian, L. Linhart, P. Rickhaus, L. Wernli, K. Watanabe, T. Taniguchi, D. Sánchez, J. Burgdörfer *et al.*, Topologically nontrivial valley states in bilayer graphene quantum point contacts, Phys. Rev. Lett. **121**, 257702 (2018).

[27] R. Kraft, I. V. Krainov, V. Gall, A. P. Dmitriev, R. Krupke, I. V. Gornyi, and R. Danneau, Valley subband splitting in bilayer graphene quantum point contacts, Phys. Rev. Lett. **121**, 257703 (2018).

[28] A. Knothe and V. Fal'ko, Influence of minivalleys and Berry curvature on electrostatically induced quantum wires in gapped bilayer graphene, Phys. Rev. B **98**, 155435 (2018).

[29] T. L. M. Lane, A. Knothe, and V. I. Fal'ko, Semimetallic features in quantum transport through a gate-defined point contact in bilayer graphene, Phys. Rev. B **100**, 115427 (2019).

[30] L. Banszerus, B. Frohn, T. Fabian, S. Somanchi, A. Epping, M. Müller, D. Neumaier, K. Watanabe, T. Taniguchi, F. Libisch *et al.*, Observation of the spin-orbit gap in bilayer graphene by one-dimensional ballistic transport, Phys. Rev. Lett. **124**, 177701 (2020).

[31] Y. Lee, A. Knothe, H. Overweg, M. Eich, C. Gold, A. Kurzmann, V. Klasovika, T. Taniguchi, K. Wantanabe, V. Fal'ko *et al.*, Tunable valley splitting due to topological orbital magnetic moment in bilayer graphene quantum point contacts, Phys. Rev. Lett. **124**, 126802 (2020).

[32] V. Gall, R. Kraft, I. V. Gornyi, and R. Danneau, Spin and valley degrees of freedom in a bilayer graphene quantum point contact: Zeeman splitting and interaction effects, Phys. Rev. Res. **4**, 023142 (2022).

[33] J. Pereira, F. Peeters, R. Costa Filho, and G. Farias, Valley polarization due to trigonal warping on tunneling electrons in graphene, J. Phys. Condens. Matter **21**, 045301 (2008).

[34] J. Ingla-Aynés, A. L. Manesco, T. S. Ghiasi, S. Volosheniuk, K. Watanabe, T. Taniguchi, and H. S. van der Zant, Specular electron focusing between gate-defined quantum point contacts in bilayer graphene, Nano Lett. **23**, 5453 (2023).

[35] L. W. Molenkamp, A. A. M. Staring, C. W. J. Beenakker, R. Eppenga, C. E. Timmering, J. G. Williamson, C. J. P. M. Harmans, and C. T. Foxon, Electron-beam collimation with a quantum point contact, Phys. Rev. B **41**, 1274 (1990).

[36] A. Yacoby, U. Sivan, C. P. Umbach, and J. M. Hong, Interference and dephasing by electron-electron interaction on length scales shorter than the elastic mean free path, Phys. Rev. Lett. **66**, 1938 (1991).

[37] K. L. Shepard, M. L. Roukes, and B. P. Van der Gaag, Direct measurement of the transmission matrix of a mesoscopic conductor, Phys. Rev. Lett. **68**, 2660 (1992).

[38] A. W. Barnard, A. Hughes, A. L. Sharpe, K. Watanabe, T. Taniguchi, and D. Goldhaber-Gordon, Absorptive pinhole collimators for ballistic dirac fermions in graphene, Nat. Commun. **8**, 15418 (2017).

[39] See Supplemental Material at http://link.aps.org/supplemental/10.1103/PhysRevLett.133.156301, which includes Refs. [16,34–37,40–46], for additional information about the V_{bg}, V_{tg}, and temperature dependence of the collimation spectra, results on a second QPC pair, and a detailed discussion of the semiclassical simulations.

[40] M. Topinka, B. J. LeRoy, S. Shaw, E. Heller, R. Westervelt, K. Maranowski, and A. Gossard, Imaging coherent electron flow from a quantum point contact, Science **289**, 2323 (2000).

[41] A. B. Kuzmenko, I. Crassee, D. Van Der Marel, P. Blake, and K. S. Novoselov, Determination of the gate-tunable band gap and tight-binding parameters in bilayer graphene using infrared spectroscopy, Phys. Rev. B **80**, 165406 (2009).

[42] M. Lee, J. R. Wallbank, P. Gallagher, K. Watanabe, T. Taniguchi, V. I. Fal'ko, and D. Goldhaber-Gordon, Ballistic miniband conduction in a graphene superlattice, Science **353**, 1526 (2016).

[43] A. A. Kozikov, D. W. Horsell, E. McCann, and V. I. Fal'Ko, Evidence for spin memory in the electron phase coherence in graphene, Phys. Rev. B **86**, 045436 (2012).

[44] L. Molenkamp, M. Brugmans, H. Van Houten, and C. Foxon, Electron-electron scattering probed by a collimated electron beam, Semicond. Sci. Technol. **7**, B228 (1992).

[45] E. H. Hwang and S. D. Sarma, Acoustic phonon scattering limited carrier mobility in two-dimensional extrinsic graphene, Phys. Rev. B **77**, 115449 (2008).

[46] J. Dunham, The Wentzel-Brillouin-Kramers method of solving the wave equation, Phys. Rev. **41**, 713 (1932).

[47] J. Ingla-Aynés, A. Manesco, T. S. Ghiasi, W. Kenji, T. Takashi, and H. S. J. van der Zant, Data underlying the publication: A ballistic electron source with magnetically-controlled valley polarization in bilayer graphene, 10.4121/8bff6fc3-91d4-4bed-8f32-e36d1b2c1fbe (2023).

[48] M. Büttiker, Four-terminal phase-coherent conductance, Phys. Rev. Lett. **57**, 1761 (1986).

[49] M. Buttiker, Symmetry of electrical conduction, IBM J. Res. Dev. **32**, 317 (1988).

[50] D. Bandurin, I. Torre, R. K. Kumar, M. Ben Shalom, A. Tomadin, A. Principi, G. Auton, E. Khestanova, K. Novoselov, I. Grigorieva *et al.*, Negative local resistance caused by viscous electron backflow in graphene, Science **351**, 1055 (2016).

[51] J. Estrada-Alvarez, F. Domínguez-Adame, and E. Díaz, Meta-hydrodynamic routes to viscous electron flow, arXiv:2306.16210.

[52] A. Rycerz, J. Tworzydło, and C. Beenakker, Valley filter and valley valve in graphene, Nat. Phys. **3**, 172 (2007).

[53] C. Tong, A. Kurzmann, R. Garreis, W. W. Huang, S. Jele, M. Eich, L. Ginzburg, C. Mittag, K. Watanabe, T. Taniguchi *et al.*, Pauli blockade of tunable two-electron spin and valley states in graphene quantum dots, Phys. Rev. Lett. **128**, 067702 (2022).

[54] R. Pisoni, Y. Lee, H. Overweg, M. Eich, P. Simonet, K. Watanabe, T. Taniguchi, R. Gorbachev, T. Ihn, and K. Ensslin, Gate-defined one-dimensional channel and broken symmetry states in MoS_2 van der Waals heterostructures, Nano Lett. **17**, 5008 (2017).

[55] K. Sakanashi, P. Kruger, K. Watanabe, T. Taniguchi, G.-H. Kim, D. K. Ferry, J. P. Bird, and N. Aoki, Signature of spin-resolved quantum point contact in p-type trilayer WSe_2 van der Waals heterostructure, Nano Lett. **21**, 7534 (2021).

[56] K. Huang, H. Fu, K. Watanabe, T. Taniguchi, and J. Zhu, High-temperature quantum valley Hall effect with quantized resistance and a topological switch, Science **385**, 657 (2024).

[57] K. Davydov, X. Zhang, W. Ren, M. Coles, L. Kline, B. Zucker, K. Watanabe, T. Taniguchi, and K. Wang, Easy- to-configure zero-dimensional valley-chiral modes in a graphene point junction, Sci. Adv. **10**, eadp6296 (2024).